ADVANCED SUSTAINABLE SYSTEMS
www.advsustainsys.com

Check for updates

A Bias-Free, Stand-Alone, and Scalable Photovoltaic–Electrochemical Device for Solar Hydrogen Production

Minoh Lee, Bugra Turan, Jan-Philipp Becker, Katharina Welter, Benjamin Klingebiel, Elmar Neumann, Yoo Jung Sohn, Tsvetelina Merdzhanova, Thomas Kirchartz, Friedhelm Finger, Uwe Rau, and Stefan Haas*

Although photovoltaic–electrochemical (PV–EC) water splitting is likely to be an important and powerful tool to provide environmentally friendly hydrogen, most developments in this field have been conducted on a laboratory scale so far. In order for the technology to make a sizeable impact on the energy transition, scaled up devices must be developed. Here a scalable (64 cm^2 aperture area) artificial PV–EC device composed of triple-junction thin-film silicon solar cells in conjunction with an electrodeposited bifunctional nickel iron molybdenum water-splitting catalyst is shown. The device shows a solar to hydrogen efficiency of up to 4.67% (5.33% active area, H_2 production rate of 1.26 µmol H_2/s) without bias assistance and wire connection and works for 30 min. The gas separation is enabled by incorporating a membrane in a 3D printed device frame. In addition, a wired small area device is also fabricated in order to show the potential of the concept. The device is operated for 127 h and initially 7.7% solar to hydrogen efficiency with a PV active area of 0.5 cm^2 is achieved.

1. Introduction

Solar powered water electrolysis is an attractive way of storing chemical energy and of supplying green hydrogen for industry as hydrogen is generated by using unlimited and clean solar energy.[1] Among the various pathways for implementation of solar–hydrogen technologies, the usage of "photovoltaic–electrochemical (PV–EC) devices," which consist of a combination of the PV device as a power source and an electrocatalyst for splitting water, can be one of the economical options to generate sustainable hydrogen.[2] In such an integrated PV–EC device, charge carriers (i.e., electrons and holes) are generated in the PV part and transferred to the electrocatalyst to split water. Several PV–EC devices have been developed using different types of PV technology, such as crystalline silicon,[3] CIGS,[4] organic–inorganic hybrid perovskite,[5] and multijunction solar cells[6] as well as different types of electrocatalyst. Although PV–EC hydrogen production has been regarded as a promising pathway in the field of hydrogen technology, most of the research has been carried out so far on a laboratory scale (≤1 cm^2). Problems that arise when scaling up PV–EC devices have hardly been tackled up to date. Our group has recently demonstrated a compact, scalable PV–EC prototype device with an aperture area of 64 cm^2. The design uses two series connected thin-film silicon a-Si:H/µc-Si:H solar cells in conjunction with a nickel foam electrocatalyst.[7] Although the scalable concept represents a critical step toward industrial application, the ≈3.9% solar-to-hydrogen (STH) efficiency of the modules must be further improved for successful commercial deployment.[2c] In addition, the concept needs to be extended to include integrated gas management for the separate collection of hydrogen and oxygen because gas mixture might cause efficiency loss from the back reactions (i.e., hydrogen oxidation and oxygen reduction reaction) and danger of a gas explosion.[8]

In the present study, we demonstrate further development of the PV–EC prototype,[7] by tackling the challenges of both low STH efficiency and lack of gas management. To increase

Dr. M. Lee, Dr. B. Turan, Dr. J.-P. Becker, Dr. K. Welter, Dr. B. Klingebiel, Dr. T. Merdzhanova, Prof. T. Kirchartz, Dr. F. Finger, Prof. U. Rau, Dr. S. Haas
IEK5 – Photovoltaik
Forschungszentrum Jülich GmbH
Jülich 52425, Germany
E-mail: m.lee@fz-juelich.de

The ORCID identification number(s) for the author(s) of this article can be found under https://doi.org/10.1002/adsu.202000070.

© 2020 The Authors. Published by WILEY-VCH Verlag GmbH & Co. KGaA, Weinheim. This is an open access article under the terms of the Creative Commons Attribution License, which permits use, distribution and reproduction in any medium, provided the original work is properly cited.

DOI: 10.1002/adsu.202000070

Dr. E. Neumann
HNF
Forschungszentrum Jülich GmbH
Jülich 52425, Germany
Dr. Y. J. Sohn
IEK1
Forschungszentrum Jülich GmbH
Jülich 52425, Germany
Prof. T. Kirchartz
Faculty of Engineering and CENIDE
University of Duisburg-Essen
Carl-Benz-Str. 199, Duisburg 47057, Germany

the efficiency of water splitting, we adapted the PV part of the device to the needs of the EC part by using efficient triple-junction solar cells based on an a-Si:H/a-Si:H/μc-Si:H layer stack as it has already been done for small (0.5 cm^2)[9] and prototype (64 cm^2)[10] scale devices. The introduction of a triple-junction Si solar cell offers the possibility of manufacturing a self-contained base unit without the need for additional series interconnection, which is normally required when using single- or double-junction solar cells.[7] This saves costs and increases the PV active area, as the interconnection creates a dead area.[11] Additionally, we developed a bifunctional NiFeMo water-splitting catalyst prepared by electrodeposition. The bifunctional catalysts enable the PV–EC system to get rid of the need for two different catalyst materials for the anode and cathode side, which offers the potential for lower costs of catalyst production and system configuration.[12] Moreover, we have developed a 3D printed frame, on which the gas separation membrane, the PV module, and the catalysts can be mounted. In addition, the gas and electrolyte management of the modules, including the gas separation, was implemented in the frame of the modules that would prevent undesired side reaction and explosion. The upscaled PV–EC device yields a STH efficiency of 4.67% with PV aperture area of 64 cm^2 (5.33% on the PV active area of 56 cm^2) but failed after 30 min. However, the failure was due to the use of improper supporting components (e.g., unsuitable adhesive between device body and back cover glass) and unfavorable design of the gas separation (e.g., curved structure of the membrane) in the integrated device rather than degradation of the photovoltaic part or the catalysts. Therefore, we believe that our scalable device concept can also achieve a high level of stability if the aforementioned problems are addressed.

2. Result and Discussion

2.1. Preparation of Triple-Junction Thin-Film Si Solar Cells

Many research groups have extensively investigated the application of multijunction cell structures consisting of vertically integrated amorphous (a-Si) and microcrystalline (μc-Si) layers for solar water splitting.[13] Such a vertically integrated multijunction structure provides an advantage of an open-circuit voltage in a wide range from 1.5 to 2.8 V that is high enough to split water[9,10b] (thermodynamic water-splitting potential; ΔE_{thermo} = 1.23 V). Therefore, the multijunction structure does not need a lateral series connection of subcells, which is a general approach to generate an affordable voltage in the PV-based spontaneous water-splitting system.[3,5] In the present work, we have used triple-junction a-Si:H/a-Si:H/μc-Si:H solar cells for the integrated solar water-splitting device since a previous report shows best STH efficiency of 9.5% for thin-film silicon solar cells in this configuration due to maximum utilization of the sun spectrum under the constraint of the need for voltages > 1.6 V.[9]

Figure 1a shows the schematic structure of a triple-junction solar cell, as investigated in the present study. We prepared three types of samples, "sample A (2.25 cm^2 active area)" without intermediate reflecting (IR) layer and "sample B (2.25 cm^2 active area)" and "sample C (0.5 cm^2 active area)" with n-type μc-SiO_x:H IR layer between the middle and the bottom cell to reduce the current mismatch between the subcells and thus increase the total current of the device.[9,14] The *I–V* characteristic of the solar cells is shown in Figure 1b (PV parameters of three types of samples can be found in Table S1, Supporting Information). The average value of solar to electricity conversion efficiency of the "sample B" (10.83%) and "sample C" (10.87%) could be increased compared to that of "sample A" (9.47%). A significant increase in the current density (from 6.41 to 7.29 and 7.21 mA cm^{-2}, respectively) seems to be the main reason for the enhancement of cell efficiency, which was achieved by introducing an IR layer. The open-circuit voltage V_{oc} of the devices is almost identical (2.14 vs 2.15–2.16 V).

2.2. Development of Electrodeposited Bifunctional NiFeMo Water-Splitting Catalyst

The efficient catalysts are required to accelerate the slow electron-transfer processes during water splitting. Although

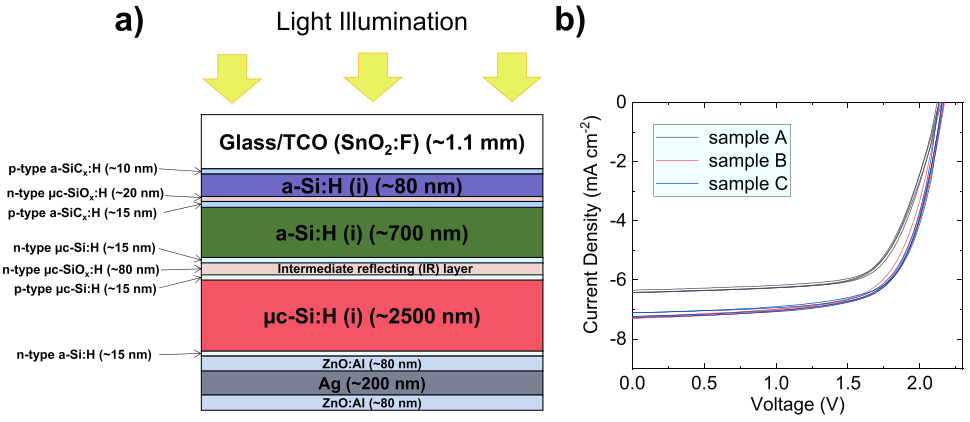

Figure 1. Characteristics of triple-junction a-Si:H/a-Si:H/μc-Si:H solar cell. a) Schematic image of the triple-junction a-Si:H/a-Si:H/μc-Si:H solar cell in a superstrate configuration. b) *I–V* characteristics of samples prepared without intermediate reflecting (IR) layer (sample A) and with IR layer (sample B and C). After introducing an IR layer, the current density was increased from 6.41 mA cm^{-2} (sample A; 2.25 cm^2 without IR layer) to 7.29 mA cm^{-2} (sample B; 2.25 cm^2 with IR layer) and 7.21 mA cm^{-2} (sample C; 0.5 cm^2 with IR layer), resulting in an increase of the average value of solar to electricity conversion efficiency from 9.47% (sample A) to 10.83% (sample B) and 10.87% (sample C).

© 2020 The Authors. Published by WILEY-VCH Verlag GmbH & Co. KGaA, Weinheim

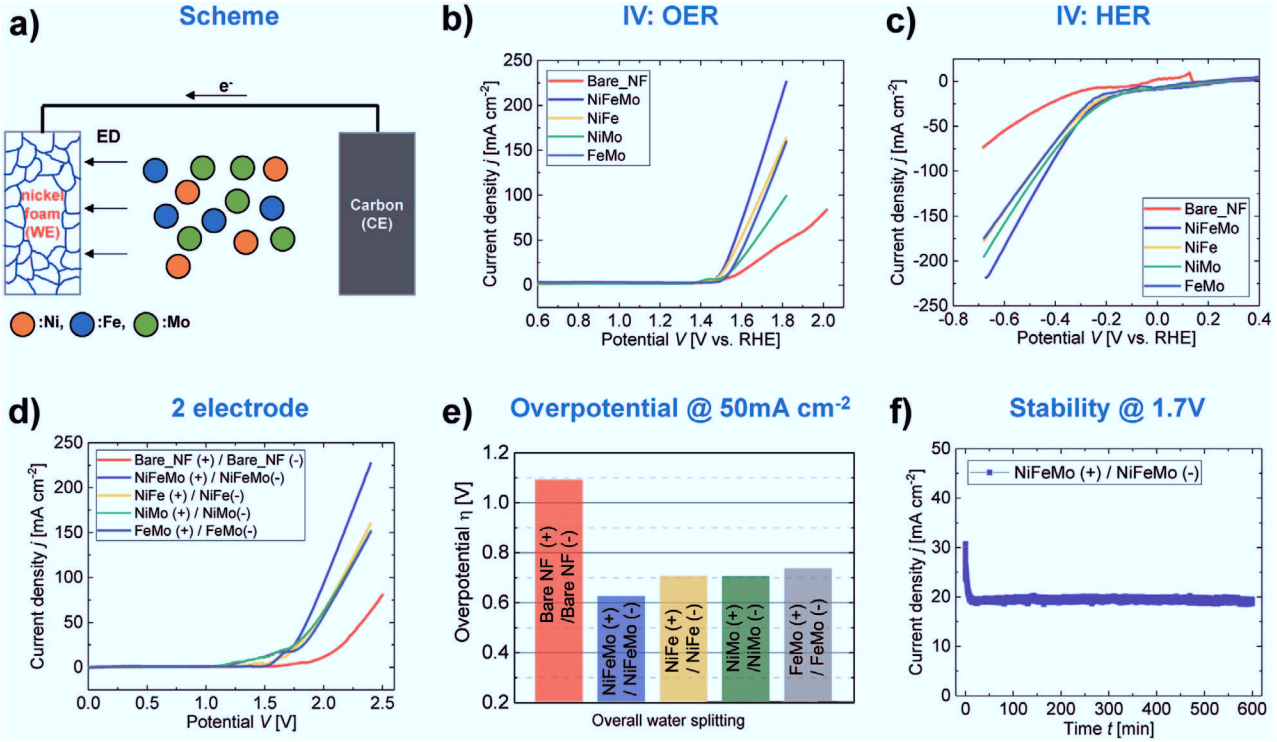

Figure 2. Electrochemical characterization of bifunctional NiFeMo electrocatalyst. a) Schematic illustration of the electrodeposition method for the preparation of NiFeMo catalyst. ED indicates electrodeposition. b–d) Linear sweep voltammetry (LSV) curves of Bare_NF (bare nickel foam), NiFeMo, NiFe, NiMo, and FeMo for different reaction modes: b) Oxygen evolution reaction (OER), c) Hydrogen evolution reaction (HER), d) Overall water splitting using each material as a bifunctional electrocatalyst in a two-electrode configuration. Notably, all the catalysts are prepared on NF. e) Comparison of overpotential with prepared samples at a current density $J = 50$ mA cm^{-2}. f) Chronoamperometry measurement of water-splitting employing NiFeMo as a bifunctional catalyst in a two-electrode system under an applied voltage of 1.7 V. All tests were conducted in 1.0 M KOH at room temperature.

noble metals and their compounds (e.g., Pt-group metals for hydrogen evolution reaction (HER) and IrO_x, RuO_x for oxygen evolution reaction (OER)) are typically used as the benchmark electrocatalysts,[15] their high price and scarcity could lead to considerable obstacles for the large technological implementation of water electrolysis systems for energy storage.[16] In order to find alternatives to the use of precious metal-based catalysts, considerable research has been undertaken into the development of electrocatalysts in the alkaline electrolyte that provides an opportunity to use earth-abundant materials (e.g., Ni, Co, Mo, etc., and their compounds/mixture).[12b,c,16b] In this study, we successfully developed an electrodeposited bifunctional electrocatalyst consisting of a NiFeMo compound for alkaline water electrolysis, which was inspired by previous research.[10a,12a,15a,17]

A schematic illustration of the electrodeposition process is presented in **Figure 2**a. Trimetal NiFeMo catalysts (or other bimetallic samples; NiFe, NiMo, FeMo) were prepared on a nickel foam (NF) substrate. We decided to use NF in this stage due to its high surface area.[18] The deposition takes place in an ammonia solution consisting of 2.4 M $NiSO_4 \cdot 6H_2O$, 0.6 M $FeSO_4 \cdot 6H_2O$, 0.2 M $Na_2MoO_4 \cdot 2H_2O$, and 0.3 M $Na_3C_6H_5O_7 \cdot 2H_2O$ at a continuous cathodic current of –160 mA cm^{-2} in a two-electrode configuration. For comparison, bimetallic samples (NiFe, NiMo, FeMo) were prepared in a similar manner. More details are provided in the Experimental Section of the Supporting Information. To investigate the electrocatalytic properties of the as-prepared samples and to find optimized preparation conditions, linear sweep voltammetry (LSV) measurements were performed with the different samples in a three-electrode (for OER and HER) and a two-electrode configuration (overall water splitting) at a scan rate of 10 mV s^{-1}. First, we varied the electrodeposition time for the NiFeMo trimetal catalyst to find empirically the optimal conditions for overall water splitting (see Figure S1, Supporting Information). Figure S1 (Supporting Information) shows the average overpotentials at a current density of 50 mA cm^{-2} as a function of the electrodeposition time for a) OER, b) HER, and c) overall reaction. Note that the potential at 50 mA cm^{-2} was chosen for the more reliable comparison between electrocatalysts since capacitance peaks (e.g., metal oxidation) were observed before reaching at water-splitting potential in Figure 2. Although the optimal deposition times for each half reaction are different (3 min for OER a) and 5 min for HER b)) we selected samples with 5 min deposition time for the integration into PV–EC devices, since the overall reaction c) performs best at 5 min. For the comparison, bimetallic samples (NiFe, NiMo, FeMo) were also prepared with a similar process; at the same time (5 min) with different precursor solution (see Figure S2 and Table S2, Supporting Information). The current density was found to depend on the catalyst deposition time. This phenomenon can be elucidated by a catalyst loading-activity relationship.[19] In particular, a better (or similar)

© 2020 The Authors. Published by WILEY-VCH Verlag GmbH & Co. KGaA, Weinheim

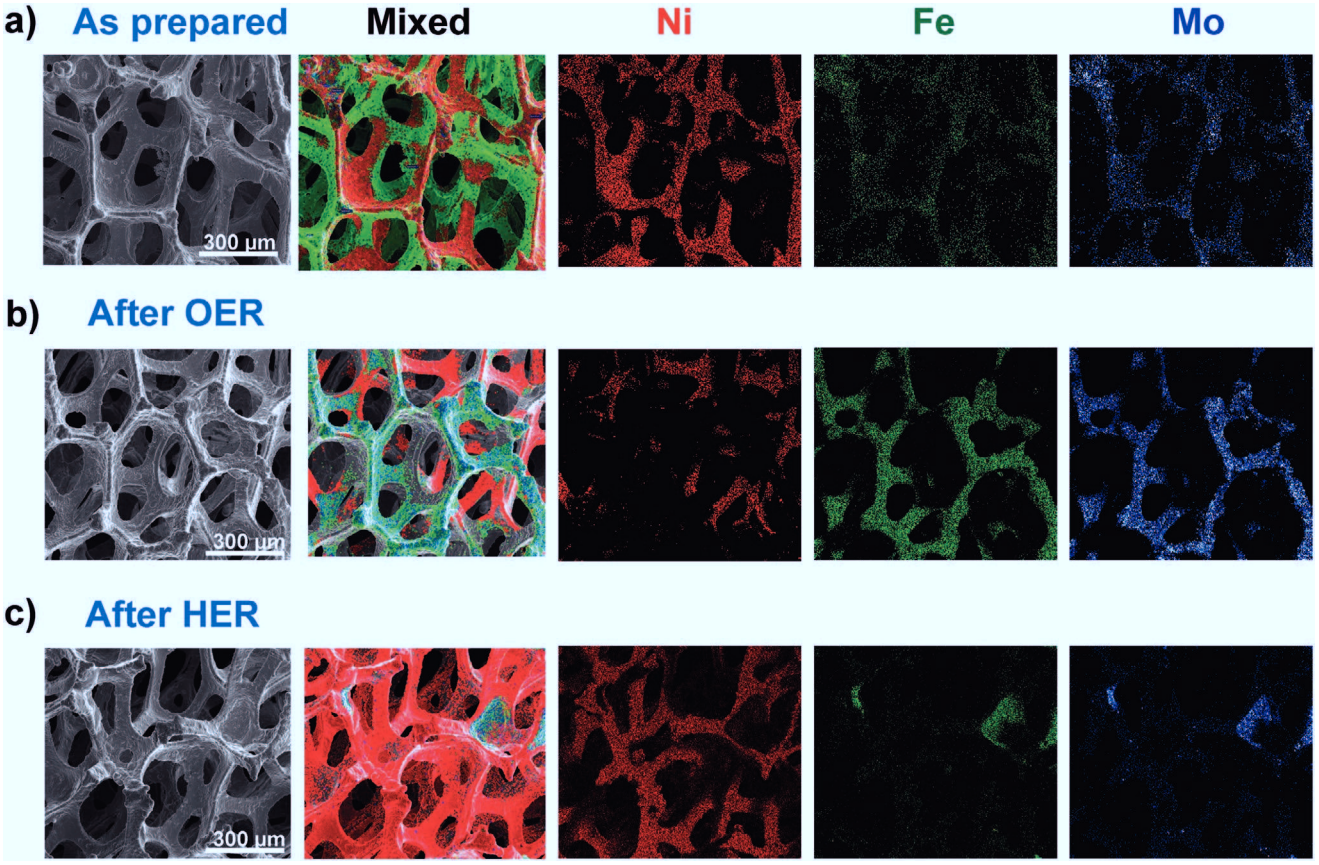

Figure 3. Comparison of the composition of bifunctional NiFeMo catalysts; a) as prepared, b) after OER (LSV measurement), and c) after HER (LSV measurement). The arrangement of images in each subsection is in the following order (from left to right); SEM image, EDS images for the mixture, Ni, Fe, and Mo. The rearrangement of the catalyst elements was observed after water-splitting reaction, implying real active sites in the water splitting might be different compared to as-prepared states.

performance was found with increasing deposition time up to 5 min (see Figure S1, Supporting Information), while the films with thickness above the optimum (deposition times > 5 min) do not guarantee higher activity than thinner films (deposition times ≤5 min). Probably the increased series resistance hinders charge transport during water splitting. Figure 2b–d shows the representative polarization curves for the different catalysts in the OER (Figure 2b), HER (Figure 2c), and overall reaction (Figure 2d). Additionally, the overall reaction overpotential at a current density of 50 mA cm^{-2} is plotted in Figure 2e. Among all samples, trimetal NiFeMo exhibits the lowest overpotential value of 0.62 V, which is considerably lower than that of the bare sample (≈1.1 V), but also slightly lower than those of the bimetallic samples (≈0.7–0.74 V). A measurement of the stability (Figure 2f) in a continued chronoamperometry test at 1.7 V, which is positioned at near maximum power point V_{mpp} of PV, for 10 h shows almost no degradation.

Figure 3a shows a large area scanning electron microscope (SEM) image and corresponding energy dispersive X-ray spectrometer (EDX) elemental mapping in which all the elements are quite uniformly distributed over hundreds of micrometers. Interestingly, the different elemental distributions of Ni, Fe, and Mo are clearly observed for the samples before and after reactions (Figure 3b,c). Note that EDX spectrums are measured at 4 different points before and after reactions (Figures S3–S5, Supporting Information) where the different peaks of Ni, Fe, and Mo are well separated in the spectrums.[17c,20] In the case of OER, the dominant distribution of Fe and Mo is clearly distinctive in EDX element mapping images. On the other hand, elemental Ni was found to be dominant after HER in which Fe and Mo seem to have disappeared (or reduced). The rearrangement of the catalyst elements after both reactions can be elucidated by a field-induced cation migration or a dissolution–precipitation mechanism.[21] These results imply real active sites involved in water-splitting reaction would be different from the as-prepared state while keeping the activities stable.

Grazing incidence X-ray diffraction (GIXRD) was analyzed as seen in Figure S6 (Supporting Information) for as-prepared NiFeMo and samples after both reactions (OER and HER). All the samples measured with an incident angle of 2°, and even with a significantly lower angle of 0.1°, show no distinct peaks apart from the Ni substrate peaks.[22] The coexistence of Ni, Fe, and Mo was confirmed by surface-sensitive X-ray photoelectron spectroscopy (XPS) measurement (Figures S7–S10, Supporting Information). All the elements were mostly found to be in a high oxidation state for the Ni (2+), Fe (3+), and Mo (6+), even in the as-prepared sample. Combining the XPS data with GIXRD results, we assume an amorphous structure of Ni, Fe, and Mo is

© 2020 The Authors. Published by WILEY-VCH Verlag GmbH & Co. KGaA, Weinheim

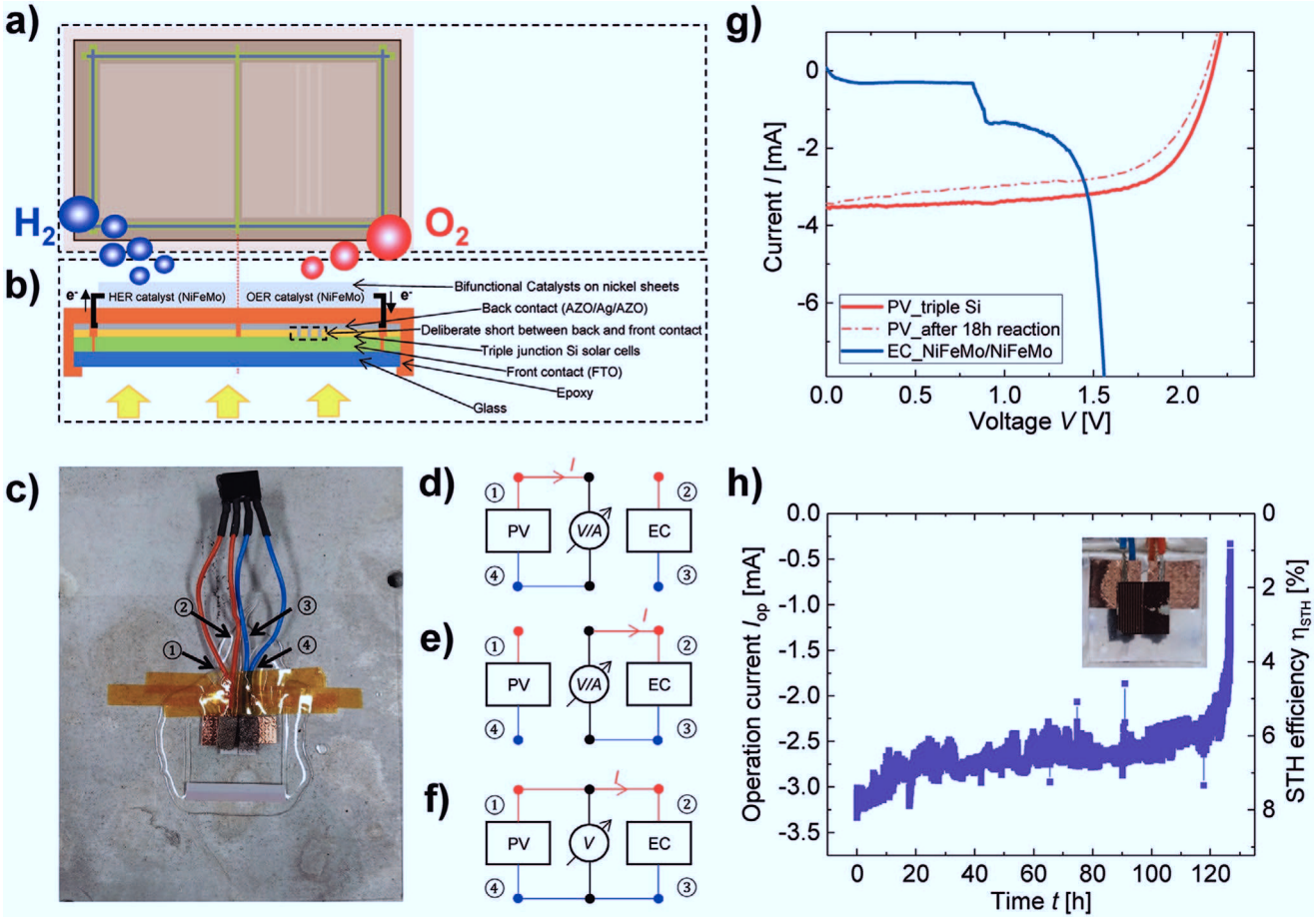

Figure 4. Wired PV–EC device on small area (PV: 0.5 cm^2 as the photoactive area, EC: both 0.5 cm^2). The schematic a) plain and b) cross-sectional view of PV–EC device and c) corresponding photograph of the lab scaled device where bifunctional NiFeMo catalysts (on both OER and HER side) were placed side-by-side on the back side of the triple-junction Si solar cell. AZO and FTO indicate aluminum doped ZnO (ZnO:Al) and fluorine doped tin oxide (SnO_2:F), respectively. Block diagram of the PV–EC device as described in (c) and different operation modes for d) PV, e) EC, and f) combined PV–EC. Characterization of small area PV–EC device. g) *I–V* characteristics of PV and EC cell in a two-electrode system. h) Chronoamperometry of PV–EC device under bias-free ($V = 0$) condition. Inset image represents a photograph of PV–EC device after continuous ≈127 h reaction. All tests were conducted in 1.0 M KOH at room temperature.

distributed in the samples. The amorphous phase might be one of the reasons for enhancing the performance of the water-splitting reaction since numerous defects could become active sites in the reaction.[12d,23] Further investigations would be required to understand the detailed relationship between mixed metals and their oxidation states, which would be required to reach firm conclusions about the nature of the active sites involved in the water-splitting reaction.

2.3. Wired PV–EC Device on Small Area (PV: 0.5 cm^2 as the Photoactive Area, EC: Both 0.5 cm^2, Ratio of PV to OER Catalyst and PV to HER Catalyst: 1)

Before the development of the upscaled device, small area PV–EC devices were fabricated, which consist of one base unit of the upscaled device. A triple-junction a-Si:H/a-Si:H/μc-Si:H solar cell and a bifunctional NiFeMo water-splitting catalyst were combined in a lateral side-by-side configuration for the base unit. The schematics in different views (plain (**Figure 4**a) and cross-sectional (Figure 4b)) and photograph (Figure 4c) of the integrated PV–EC device are provided in Figure 4a–c, respectively. Superstrate configuration of solar cells provides a better light absorbing path without inevitable loss from interruption of catalysts and bubbles, which are issues that commonly used water-splitting systems are facing.[13g,24] Wires (used here only to measure the current and voltages of PV and EC, separately) were connected to the contacts of the PV cell by fixing them with copper tape and to the contacts of the EC cell by soldering with tin. We made separate contacts of the PV part and the EC part to allow for individual measurement of the *I*/*V*-characteristics.

Figure 4d–f shows the illustration images of the block diagram with the different operation mode of the PV–EC device, thereby, both current and voltage can be measured in this configuration. The performance of an integrated PV–EC device fixed into a well-sealed polyether ether ketone (PEEK) device holder was evaluated (see Figure S12b, Supporting Information). The individual *I–V* curves of PV and EC are shown in Figure 4g. The PV delivers an open-circuit voltage V_{oc} of about 2.16 V and a voltage at the maximum power point V_{mpp} of about

© 2020 The Authors. Published by WILEY-VCH Verlag GmbH & Co. KGaA, Weinheim

1.72 V, which is sufficiently high to enable bias-free water splitting. The intersection point, where both *I–V* curves of PV and EC meet, is considered as the operation current of the integrated PV–EC device without any assistance of bias. The intersection point is located at a current of −3.2 mA, corresponding to an active area STH efficiency of 7.87% (calculated with Equation (S1), see the Supporting Information). Here, we have used the photoactive area (left-hand side, 0.5 cm^2) not considering anode dead area (right-hand side) where front- and back-contacts are deliberately shorted. The operation current of an integrated PV–EC device was continuously monitored over 127 h and plotted in Figure 4h. The average STH efficiency for the first 1 h was determined to be 7.72%, which is in good agreement with the predicted value of 7.87%. The performance gradually degraded over 18 h. After removing the electrolyte, the *I–V* characteristic of the PV part was measured. Although both current and voltage of the PV part are not far from the original values, a significant reduction of the fill factor was observed (see Figure 4g), which can be linked to the light instability of amorphous thin-film Si (Staebler–Wronski effect).[25] The measurement was resumed with a refreshed electrolyte, and operation current was partially recovered and then gradually decreased until the device failed. Around 6.4% STH efficiency was achieved after 100 h (calculated from the average current for 1 h; 99–100 h) with 17% decrease from the initial value. Previously it was shown that ≈100 h continuous light illumination induces degradation of ≈12% in solar to electricity conversion efficiency of triple-junction a-Si:H/a-Si:H/μc-Si:H solar cell,[26] which can be a primary factor for the degradation of the integrated PV–EC device. Additionally, an increase in the coupling losses (e.g., wire and contact resistances) or partial degradation of the catalysts during the reaction may lead to the STH efficiency decrease. Beside that, mass transport limitation cannot be ruled out in the device performance.[27] Ionic concentration gradient can be possibly formed during operation since we have used 1 M KOH solution that is not sufficient compared to highly concentrated solution (6 M KOH) used in commercial electrolyzers. The device fully failed after around 127 h. Probably the epoxy was not stable for such a prolonged time, enabling hydroxide ion permeation to the silicon layer (see the inset in Figure 4h).

2.4. Wireless PV–EC Device in a Prototype Scale (PV: 64 cm^2 Aperture Area, 56 cm^2 Active Area, EC: Both 26.1 cm^2, Ratio of PV to OER Catalyst and PV to HER Catalyst: 2.15)

The upscaled PV–EC device concept was realized in a 3D printed frame made of Digital ABS Plus material, which acts as a support for the PV module, the catalysts, and the membrane (see **Figure 5**b). The use of the membrane inhibits potential losses from back reactions, such as hydrogen oxidation and oxygen reduction reaction.[8a] The risk of explosion from the accumulation of gas mixture can also be prevented by introducing a membrane.[8a] In addition, gas management is implemented in the frame by several gas pipes. Both chamber types are additionally connected to the outside to allow a separate collection of the gases. Furthermore, pipes at the bottom of the frame can be used to replace used electrolyte. For the upscaled device, according to the previous approaches,[10] we introduced nickel sheets (NS) as a substrate for the catalyst in contrast to the NF used for the catalyst development and the small area devices. While NS has a drawback of smaller surface area, it has the advantage of being impermeable. Thus, the PV module is completely protected against corrosion from the alkaline electrolyte (see Figure 5a), while they are still in thermal contact. Allowing heat exchange between PV part and EC part, which we assume to be the case in our setup, can be beneficial in real applications regarding the STH efficiency.[28] Detailed information in terms of preparation procedure and dimensions can be found in the Supporting Information.

Figure 5a shows a schematic illustration of the upscaled PV–EC device. The base unit, which was introduced in the section of the small scale device (represented in the dashed box), is continuously repeated to cover larger areas. Seven adjoining base units consisting of triple-junction a-Si:H/a-Si:H/μc-Si:H solar cells and bifunctional NiFeMo water-splitting catalyst were used. The upscaled wireless PV–EC device cannot be explored by measuring the current for the calculation of STH efficiency. To evaluate the performance of the device, the produced amount of hydrogen and oxygen was monitored over time instead of monitoring the current. Figure 5e shows the collected gas volume over time for H_2, O_2, and for the total volume. The upscaled PV–EC device yields a STH efficiency of up to 4.67% (5.33% active area) for the first 10 min (volume change was monitored after 5 min stabilization). Note that the collected gas was converted to STH efficiency using Equation (S2) (see the Supporting Information). Figure 5f shows the H_2 production rate and STH efficiency calculated by both total and H_2 gas. It is noteworthy that the STH efficiency calculated based on the total gas rate decreases much slower than that calculated based on the H_2 production rate. This is a clear indication for a gas crossover between the OER and the HER chambers (some H_2 moves to O_2 part). The crossover might be a result of an imperfect working anion exchange membrane due to the curved application and/or instability in the applied epoxy that glues the membranes to the 3D printed frame. The ratio of H_2 to O_2 is shown in Figure 5g. The gas ratio at the first 10 min was found to be ≈2.18, instead of the ideal value of 2. It can be assumed that the surface state of the catalyst does not reach a steady state (e.g., redox reaction, dissolution, electromigration, etc.) although we measured the gas volume after 5 min of stabilization.[21a,29] The gradual decrease observed in the ratio (from ≈2.18 to ≈1.89) can also be linked to the gas cross over mentioned above. Unfortunately, after 30 min of operation, the device failed due to a detachment of the plexiglass cover. Further improvements in the selection of adhesives as well as in the application of the anion exchange membrane are needed in order to improve the device stability. Nevertheless, we realized an increase of efficiency of around 16.5% compared to our previous result (≈3.9%),[7] where two a-Si:H/μc-Si:H tandem solar cells serially connected together with bare NF as the catalyst were used. The enhancement of the efficiency can be ascribed to a better matching of the characteristics of the PV part and the EC part. In addition, an increase of the total active area (56 vs 52.8 cm^2) for a given total aperture area (64 cm^2) by reducing the number of base units (reducing the number of inactive anode contacts) can

© 2020 The Authors. Published by WILEY-VCH Verlag GmbH & Co. KGaA, Weinheim

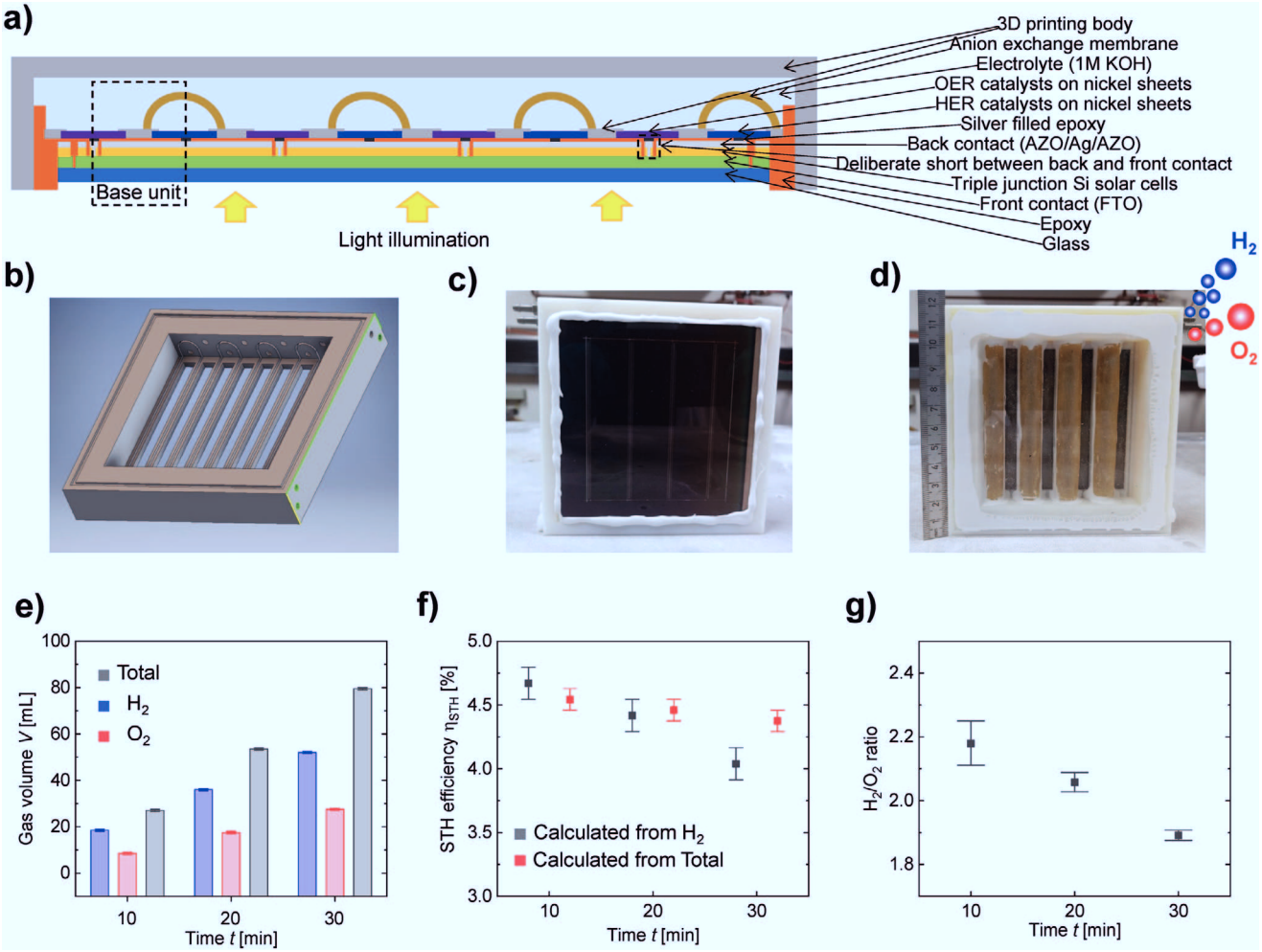

Figure 5. Wireless PV–EC device in a prototype scale (PV: 64 cm^2 aperture area, 56 cm^2 active area, EC: both 26.1 cm^2). a) Schematic illustration of an upscaled PV–EC device as used in this study. AZO and FTO indicate aluminum doped ZnO (ZnO:Al) and fluorine doped tin oxide (SnO_2:F), respectively. b) Drawing of the 3D printed frame used to hold the catalysts, the solar module, and the membranes. Additionally, the frame is used for gas management. c,d) Photographs of upscaled PV–EC prototype device; c) front side view (PV side), d) back side view (EC side) after integration of catalyst, membrane, and cover glass. e–g) Characterization of upscaled PV–EC device (direct gas measurement was conducted to evaluate STH efficiency instead of monitoring the operation current (I_{op}) since I_{op} cannot be measured in the absence of wires); The measurement error was estimated to be ±0.5 mL. e) Collected gas (H_2, O_2, and total) volume, f) Corresponding solar to hydrogen (STH) efficiency, and g) Ratio of H_2 to O_2 as a function of time.

be one of the reasons for the improvement of STH efficiency. Although the laser-generated anode connection has only a width of ≈100 µm, we need a much wider area for the anode contact (≈2 mm) due to the manual deposition of the metal filled epoxy, which connects the anode contact to the OER catalyst. Thus, there is still room for improvement of the STH efficiency by further optimizing the device manufacturing processes by using, e.g., more precise deposition techniques like inkjet printing or computer-controlled dispensing.

3. Conclusion

In this study, we successfully introduced a scalable photovoltaic–electrochemical device that incorporates gas separation and gas handling. As a power source, triple-junction thin-film silicon solar cells were used. This type of solar cells offers almost perfect voltage matching to highly active catalysts without the need for lateral series connection or even external bias. By introducing an intermediate reflecting layer into the solar device, the current density was increased from 6.41 to 7.29 mA cm^{-2}. To achieve high STH efficiencies, we additionally developed stable bifunctional (OER and HER) NiFeMo water-splitting catalysts made of inexpensive earth-abundant materials that we prepared by electrodeposition. Besides being a cost-effective route of electrodeposition for the sample preparation, the bifunctional property can additionally lower the cost of a PV–EC system, since it can be used with one type of catalyst in the same electrolyte.

By combining the triple-junction thin-film silicon solar cell with the bifunctional NiFeMo catalyst, an integrated PV–EC device with an active area of 0.5 cm^2 was realized. The device had an initial STH efficiency of ≈7.7%. After 100 h of operation, the STH efficiency was reduced by 17% (STH efficiency from 7.72% to 6.40%). Here the efficiency decrease might result

© 2020 The Authors. Published by WILEY-VCH Verlag GmbH & Co. KGaA, Weinheim

from a combination of the light induced degradation (Staebler–Wronsky effect) of the amorphous silicon layers in the solar cell, increasing coupling losses (e.g., wire and contact resistances), and partial degradation of the catalysts during the water-splitting reaction. Finally, an upscaled device with an aperture area of 64 cm² was realized. Here a 3D printed frame was used acting as a support for the PV module, the catalysts, and the membrane. In addition, gas management and gas handling were realized in the frame. The upscaled device yields an STH efficiency of 4.67% (5.33% for the active area) during the first 10 min under bias-free condition.

Supporting Information

Supporting Information is available from the Wiley Online Library or from the author.

Acknowledgements

The authors gratefully acknowledge financial support from the "PECSYS" project, which has received funding from the Fuel Cells and Hydrogen 2 Joint Undertaking under Grant Agreement No. 735218. This joint Undertaking receives support by the European Union's Horizon 2020 research and innovation programme and Hydrogen Europe and N. ERGHY. They also thank the Initiative and Networking Fund of the Helmholtz Association for funding of the JOSEPH cluster system via the Helmholtz Energy Materials Characterization Platform (HEMCP).

Conflict of Interest

The authors declare no conflict of interest.

Author Contributions

U.R., F.F., and S.H. developed the conceptual idea and supervised the work. M.L. performed the experiments, collected and analyzed the data, and prepared a draft of the manuscript. B.T., J.-P.B., K.W., B.K., E.N., Y.J.S., T.M., and T.K. performed the experimental measurements and analysis. All of the authors discussed the results and commented on the manuscript. The authors thank J. Kirchhoff, G. Schöpe, C. Zahren, S. Kasper, H. Siekmann, A. Bauer, and A. Gerber for their contributions to this work.

Keywords

electrodeposited catalysts, NiFeMo catalysts, photovoltaic–electrochemical device, thin-film solar cells, triple junction solar cells, water-splitting catalysts, water splitting

Received: March 19, 2020
Revised: April 21, 2020
Published online: May 12, 2020

[1] a) N. S. Lewis, D. G. Nocera, *Proc. Natl. Acad. Sci. USA* **2006**, *103*, 15729; b) S. Chu, W. Li, Y. Yan, T. Hamann, I. Shih, D. Wang, Z. Mi, *Nano Futures* **2017**, *1*, 022001.

[2] a) M. Reuß, J. Reul, T. Grube, M. Langemann, S. Calnan, M. Robinius, R. Schlatmann, U. Rau, D. Stolten, *Sustainable Energy Fuels* **2019**, *3*, 801; b) T. J. Jacobsson, V. Fjällström, M. Edoff, T. Edvinsson, *Energy Environ. Sci.* **2014**, *7*, 2056; c) S. Ardo, D. Fernandez Rivas, M. A. Modestino, V. Schulze Greiving, F. F. Abdi, E. Alarcon Llado, V. Artero, K. Ayers, C. Battaglia, J.-P. Becker, D. Bederak, A. Berger, F. Buda, E. Chinello, B. Dam, V. Di Palma, T. Edvinsson, K. Fujii, H. Gardeniers, H. Geerlings, S. M. H. Hashemi, S. Haussener, F. Houle, J. Huskens, B. D. James, K. Konrad, A. Kudo, P. P. Kunturu, D. Lohse, B. Mei, E. L. Miller, G. F. Moore, J. Muller, K. L. Orchard, T. E. Rosser, F. H. Saadi, J.-W. Schüttauf, B. Seger, S. W. Sheehan, W. A. Smith, J. Spurgeon, M. H. Tang, R. van de Krol, P. C. K. Vesborg, P. Westerik, *Energy Environ. Sci.* **2018**, *11*, 2768.

[3] C. R. Cox, J. Z. Lee, D. G. Nocera, T. Buonassisi, *Proc. Natl. Acad. Sci. USA* **2014**, *111*, 14057.

[4] T. J. Jacobsson, V. Fjällström, M. Sahlberg, M. Edoff, T. Edvinsson, *Energy Environ. Sci.* **2013**, *6*, 3676.

[5] J. Luo, J.-H. Im, M. T. Mayer, M. Schreier, M. K. Nazeeruddin, N.-G. Park, S. D. Tilley, H. J. Fan, M. Grätzel, *Science* **2014**, *345*, 1593.

[6] a) O. Khaselev, J. A. Turner, *Science* **1998**, *280*, 425; b) S. Y. Reece, J. A. Hamel, K. Sung, T. D. Jarvi, A. J. Esswein, J. J. H. Pijpers, D. G. Nocera, *Science* **2011**, *334*, 645; c) J. Jia, L. C. Seitz, J. D. Benck, Y. Huo, Y. Chen, J. W. D. Ng, T. Bilir, J. S. Harris, T. F. Jaramillo, *Nat. Commun.* **2016**, *7*, 13237; d) J. Gao, F. Sahli, C. Liu, D. Ren, X. Guo, J. Werner, Q. Jeangros, S. M. Zakeeruddin, C. Ballif, M. Grätzel, J. Luo, *Joule* **2019**, *3*, 2930.

[7] B. Turan, J.-P. Becker, F. Urbain, F. Finger, U. Rau, S. Haas, *Nat. Commun.* **2016**, *7*, 12681.

[8] a) M. A. Modestino, K. A. Walczak, A. Berger, C. M. Evans, S. Haussener, C. Koval, J. S. Newman, J. W. Ager, R. A. Segalman, *Energy Environ. Sci.* **2014**, *7*, 297; b) A. Berger, R. A. Segalman, J. Newman, *Energy Environ. Sci.* **2014**, *7*, 1468.

[9] F. Urbain, V. Smirnov, J.-P. Becker, A. Lambertz, F. Yang, J. Ziegler, B. Kaiser, W. Jaegermann, U. Rau, F. Finger, *Energy Environ. Sci.* **2016**, *9*, 145.

[10] a) J. P. Becker, B. Turan, V. Smirnov, K. Welter, F. Urbain, J. Wolff, S. Haas, F. Finger, *J. Mater. Chem. A* **2017**, *5*, 4818; b) K. Welter, N. Hamzelui, V. Smirnov, J. P. Becker, W. Jaegermann, F. Finger, *J. Mater. Chem. A* **2018**, *6*, 15968.

[11] Y. Gupta, H. Liers, S. Woods, S. Young, R. DeBlasio, L. Mrig, in *Proceedings of the 16th IEEE Photovoltaics Specialist Conferences*, IEEE, San Diego **1982**, p. 1092.

[12] a) F. Qin, Z. Zhao, M. K. Alam, Y. Ni, F. Robles-Hernandez, L. Yu, S. Chen, Z. Ren, Z. Wang, J. Bao, *ACS Energy Lett.* **2018**, *3*, 546; b) J. R. McKone, S. C. Marinescu, B. S. Brunschwig, J. R. Winkler, H. B. Gray, *Chem. Sci.* **2014**, *5*, 865; c) B. M. Hunter, H. B. Gray, A. M. Müller, *Chem. Rev.* **2016**, *116*, 14120; d) X. Lu, C. Zhao, *Nat. Commun.* **2015**, *6*, 6616.

[13] a) A. E. Delahoy, S. C. Gau, O. J. Murphy, M. Kapur, J. O. M. Bockris, *Int. J. Hydrogen Energy* **1985**, *10*, 113; b) C. Gramaccioni, A. Selvaggi, F. Galluzzi, *Electrochim. Acta* **1993**, *38*, 111; c) O. Khaselev, A. Bansal, J. A. Turner, *Int. J. Hydrogen Energy* **2001**, *26*, 127; d) Y. Yamada, N. Matsuki, T. Ohmori, H. Mametsuka, M. Kondo, A. Matsuda, E. Suzuki, *Int. J. Hydrogen Energy* **2003**, *28*, 1167; e) E. L. Miller, D. Paluselli, B. Marsen, R. E. Rocheleau, *Sol. Energy Mater. Sol. Cells* **2005**, *88*, 131; f) V. Cristino, S. Berardi, S. Caramori, R. Argazzi, S. Carli, L. Meda, A. Tacca, C. A. Bignozzi, *Phys. Chem. Chem. Phys.* **2013**, *15*, 13083; g) P. Bogdanoff, D. Stellmach, O. Gabriel, B. Stannowski, R. Schlatmann, R. van de Krol, S. Fiechter, *Energy Technol.* **2016**, *4*, 230.

[14] A. Lambertz, V. Smirnov, T. Merdzhanova, K. Ding, S. Haas, G. Jost, R. E. I. Schropp, F. Finger, U. Rau, *Sol. Energy Mater. Sol. Cells* **2013**, *119*, 134.

© 2020 The Authors. Published by WILEY-VCH Verlag GmbH & Co. KGaA, Weinheim

[15] a) C. C. L. McCrory, S. Jung, I. M. Ferrer, S. M. Chatman, J. C. Peters, T. F. Jaramillo, *J. Am. Chem. Soc.* **2015**, *137*, 4347; b) C. C. L. McCrory, S. Jung, J. C. Peters, T. F. Jaramillo, *J. Am. Chem. Soc.* **2013**, *135*, 16977.
[16] a) F. Song, L. Bai, A. Moysiadou, S. Lee, C. Hu, L. Liardet, X. Hu, *J. Am. Chem. Soc.* **2018**, *140*, 7748; b) N. Mahmood, Y. Yao, J.-W. Zhang, L. Pan, X. Zhang, J.-J. Zou, *Adv. Sci.* **2018**, *5*, 1700464.
[17] a) C. Fan, D. L. Piron, A. Sleb, P. Paradis, *J. Electrochem. Soc.* **1994**, *141*, 382; b) I. A. Raj, K. I. Vasu, *J. Appl. Electrochem.* **1992**, *22*, 471; c) M. Jayalakshmi, W. Y. Kim, K. D. Jung, O. S. Joo, *Int. J. Electrochem. Sci.* **2008**, *3*, 908.
[18] C. Xiao, Y. Li, X. Lu, C. Zhao, *Adv. Funct. Mater.* **2016**, *26*, 3515.
[19] C. G. Morales-Guio, L. Liardet, X. Hu, *J. Am. Chem. Soc.* **2016**, *138*, 8946.
[20] https://www.bruker.com/fileadmin/user_upload/8-PDF-Docs/X-ray-Diffraction_ElementalAnalysis/Microanalysis_EBSD/LabReports/App_eds_01_en_rev1_2_lores.pdf (accessed: April 2020).
[21] a) J. P. Singh, T. M. Lu, G. C. Wang, *Appl. Phys. Lett.* **2003**, *82*, 4672; b) H. Schäfer, S. Sadaf, L. Walder, K. Kuepper, S. Dinklage, J. Wollschläger, L. Schneider, M. Steinhart, J. Hardege, D. Daum, *Energy Environ. Sci.* **2015**, *8*, 2685.
[22] a) J. Geng, D. A. Jefferson, B. F. G. Johnson, *Chem. Commun.* **2007**, 969; b) S. Zhang, S. Gai, F. He, Y. Dai, P. Gao, L. Li, Y. Chen, P. Yang, *Nanoscale* **2014**, *6*, 7025.
[23] a) A. Bergmann, E. Martinez-Moreno, D. Teschner, P. Chernev, M. Gliech, J. F. de Araújo, T. Reier, H. Dau, P. Strasser, *Nat. Commun.* **2015**, *6*, 8625; b) C. G. Morales-Guio, X. Hu, *Acc. Chem. Res.* **2014**, *47*, 2671.
[24] C. G. Morales-Guio, M. T. Mayer, A. Yella, S. D. Tilley, M. Grätzel, X. Hu, *J. Am. Chem. Soc.* **2015**, *137*, 9927.
[25] D. L. Staebler, C. R. Wronski, *Appl. Phys. Lett.* **1977**, *31*, 292.
[26] F. Urbain, V. Smirnov, J.-P. Becker, F. Finger, *ACS Omega* **2016**, *1*, 832.
[27] a) M. A. Modestino, S. M. H. Hashemi, S. Haussener, *Energy Environ. Sci.* **2016**, *9*, 1533; b) T. Shinagawa, K. Takanabe, *ChemSusChem* **2017**, *10*, 1318.
[28] K. Welter, V. Smirnov, J.-P. Becker, P. Borowski, S. Hoch, A. Maljusch, W. Jaegermann, F. Finger, *ChemElectroChem* **2017**, *4*, 2099.
[29] C. Spöri, J. T. H. Kwan, A. Bonakdarpour, D. P. Wilkinson, P. Strasser, *Angew. Chem., Int. Ed.* **2017**, *56*, 5994.

© 2020 The Authors. Published by WILEY-VCH Verlag GmbH & Co. KGaA, Weinheim